Nano Research

Open Access

Research Article

Perovskite defect passivation for efficient photon-counting detector

Wenjie Luo[1,2,6,§], Pengshuo Gan[2,3,§], Binyun Han[2], Kaixin Huang[3], Xingzhou Su[1,2,6], Wenxuan Yang[1,2], Qing Zhong[3], Hao Huang[2], Yang Zhang[2], Xue-Feng Yu[2], Yongfeng Yang[2,4], Chang Liu[3] ✉, Zheng Liu[2,4] ✉, Wenhua Zhou[2,4] ✉, and Yanliang Liu[2,4,5] ✉

[1] *Southern University of Science and Technology, Shenzhen 518055, China*
[2] *Shenzhen Institute of Advanced Technology, Chinese Academy of Sciences, Shenzhen 518055, China*
[3] *Engineering and Research Center for Integrated New Energy Photovoltaics & Energy Storage Systems of Hunan Province, School of Electrical Engineering, University of South China, Hengyang 421001, China*
[4] *Key Laboratory of Biomedical Imaging Science and System, Chinese Academy of Sciences, Shenzhen 518055, China*
[5] *Hong Kong Institute of Science & Innovation, Chinese Academy of Sciences, Hong Kong 999077, China*
[6] *Shenzhen University of Advanced Technology, Shenzhen 518055, China*
[§] *Wenjie Luo and Pengshuo Gan contributed equally to this work.*

Cite this article: *Nano Research*, **2026**, *19*, 94908490. https://doi.org/10.26599/NR.2026.94908490

ABSTRACT: Although metal halide perovskites have advanced rapidly in photoelectrical detection, studies on perovskite-based photon-counting detector remain scarce. This study reports an efficient perovskite photon-counting detector achieved through defect passivation of the perovskite photosensitive layer. Urea, a Lewis base, was introduced as an additive during the two-step fabrication of $MAPbI_3$ films, forming a complex ($MAI{\cdot}PbI_2{\cdot}O{=}C(NH_2)_2$, where MAI = methylammonium iodide) that slowed the reaction rate and promoted complete reaction between MAI and PbI_2. Compared to conventional perovskite films, the optimized $MAPbI_3$ film exhibits enhanced crystallinity, with enlarged grain size from 254.8 to 908.1 nm, and reduced defect density from 9.08×10^{15} to 3.89×10^{15} cm^{-3}. The resulting $MAPbI_3$ photodiode detector demonstrates satisfactory performance, achieving a responsivity of 0.4 A/W and a sensitivity of 2.39×10^{13} Jones under 17.02 μW/cm^2 illumination. Furthermore, a photon-counting system integrated with the $MAPbI_3$ photodetector was able to detect low light levels down to 2.01×10^3 photons per mm^2, with a photoresponse three times higher than that of silicon-based photon-counting detector.

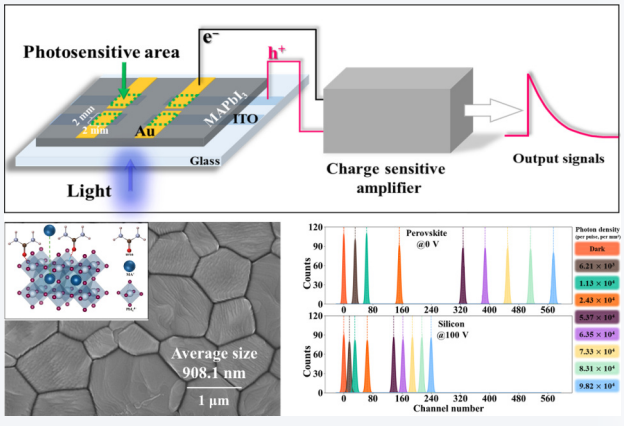

KEYWORDS: $MAPbI_3$ perovskite, photon-counting detectors, modification, defect passivation

1 Introduction

The photon-counting detector, which converts light signals into electrical signals, is widely used in single-molecule detection, fluorescence spectral imaging, medical imaging, and optoelectronic communications [1, 2]. When semiconductor materials are exposed to electromagnetic radiation, the resulting electric field separates electron–hole pairs within the materials, generating an electrical signal proportional to the energy of the incident radiation [3, 4]. Although commercial silicon-based photon-counting detectors have undergone extensive development in recent years, the indirect bandgap of silicon introduces several limitations, including low absorption coefficients, a narrow spectral response range, high noise levels, and the requirement for cryogenic operation to mitigate noise. Additionally, silicon photon-counting detectors surfer from issues such as complex manufacturing processes, high costs, limited mechanical flexibility, and performance constraints [5]. Therefore, developing new semiconductor materials for photon-counting detectors is essential for advancing detection capabilities.

Metal halide perovskites have rapidly emerged as promising materials in field of optoelectronics [6–8] due to their excellent properties, such as high optical absorption coefficients [9–14], high

Received: December 10, 2025; **Revised:** January 6, 2026
Accepted: January 25, 2026

✉Address correspondence to Yanliang Liu, yl.liu4@siat.ac.cn; Wenhua Zhou, wh.zhou@siat.ac.cn; Zheng Liu, zheng.liu@siat.ac.cn; Chang Liu, liuchang@usc.edu.cn

charge carrier mobility [15–18], long charge carrier diffusion lengths [19–21], low exciton binding energies [22], and tunable direct bandgaps [23–26]. In addition, perovskites offer advantages such as low manufacturing costs and processing flexibility. These exceptional characteristics highlight the great potential of perovskite materials for optoelectronic detection applications. In 2023, Huang's research group reported the first successful development of a perovskite-based photon-counting detector, demonstrating excellent performance [27]. However, solution-processed perovskite films often introduce crystal defects, and consequently, various optimization strategies have been developed to improve film quality, leading to advancements in solar cells, light-emitting diodes (LEDs), and photodetectors [28–32]. Nonetheless, research specifically focusing on photon-counting detectors remains limited. The quality of perovskite films is critical to the overall performance of photon-counting detectors, as defects within the perovskite materials can trap free charges and alter recombination pathways, thereby influencing optoelectronic processes. High defect density may lead to non-radiative recombination [33], charge trapping [34], charge scattering [35], and ionic migration [36], severely degrading the optoelectronic performance of the photon-counting detector. In mature inorganic photon-counting semiconductor materials such as silicon and GaAs, effective defect control and optimization have been the key to their rapid development [37–39]. Therefore, further investigation into the impact of defects in the perovskite films on the photon-counting performance of perovskite photodetectors is of great significance.

In this study, we report an efficient perovskite photon-counting detector based on a two-step fabricated $MAPbI_3$ film. Urea, a Lewis base, was introduced as an additive to improve the optoelectronic properties of the perovskite films. Urea forms an intermediate complex ($MAI{\cdot}PbI_2{\cdot}O{=}C(NH_2)_2$, where MAI = methylammonium iodide), slowing the reaction rate and promoting a more complete reaction between MAI and lead iodide (PbI_2). The optimized $MAPbI_3$ film exhibits enhanced crystallinity, with grain size increasing from 254.8 to 908.1 nm, and a reduced defect density from 5.98×10^{15} to 4.05×10^{15} cm^{-3} compared to conventional perovskite film. As a result, the urea-optimized $MAPbI_3$ film exhibited significantly improved photodetection performance, achieving a responsivity of 0.4 A/W and a specific detectivity of 2.39×10^{13} Jones under 17.02 μW/cm^2 illumination. Furthermore, the perovskite detector was applied to photon counting, achieving a minimum detectable photon flux of 2.01×10^3 photons per mm^2, and its photoresponse was three times higher than that of a silicon photon-counting detector under same photon flux.

2 Results and discussion

2.1 Structural and morphology of perovskite photon-counting detectors

The schematic of the perovskite photon-counting detector is illustrated in Fig. 1(a) (the physical setup of the experiment is shown in Fig. S1 in the Electronic Supplementary Material (ESM)). Upon photoelectric conversion in the perovskite photosensitive layer, the generated electron–hole pairs are transferred to a charge-sensitive amplifier through different electrodes. After amplification, the output pulse signal reflects the photon-counting response of the detector. The output response pulse histograms of the perovskite photon-counting detector fabricated using conventional $MAPbI_3$ photosensitive layers at zero bias are shown in Fig. 1(b). The figure shows that the minimum detectable photon count, defined as the incident photon count at which the output response becomes completely distinguishable from the dark noise response, is 5.69×10^3 photon/mm^2. However, the photon-counting limit of the conventional $MAPbI_3$ detector remains inadequate to meet the performance requirements of most photon-counting applications. As previously reported, shallow defects located at perovskite grain boundaries influence the photon-counting detector performance [27]. Therefore, further passivation of the crystal defects in perovskite films and reduction of defect state density are essential for suppressing dark noise and enhancing the detection efficiency of perovskite photon-counting detectors.

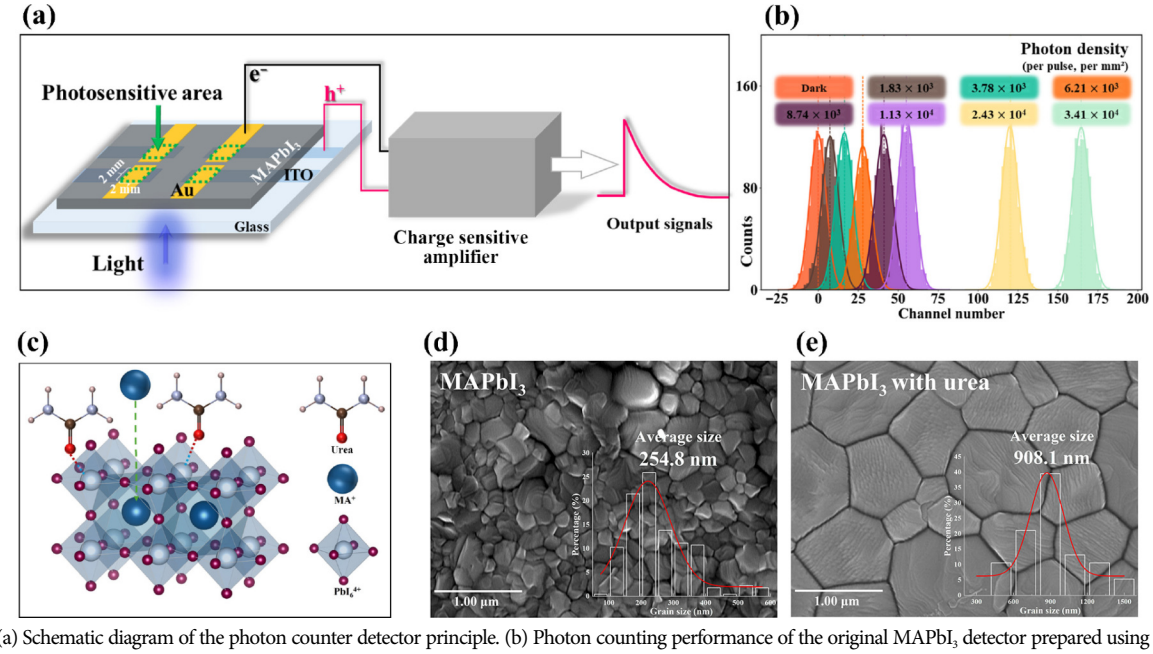

Figure 1 (a) Schematic diagram of the photon counter detector principle. (b) Photon counting performance of the original $MAPbI_3$ detector prepared using the two-step method. (c) Schematic diagram showing the role of urea in the crystallization of perovskite films. ((d) and (e)) SEM images of perovskite film surfaces treated (d) without urea and (e) with urea.

In the two-step fabrication process of $MAPbI_3$ film, a PbI_2 solution is first spin-coated and annealed to form a compact thin film. Subsequently, an MAI solution is introduced to react with the PbI_2 film, resulting in the formation of $MAPbI_3$. Typically, MAI infiltrates the PbI_2 film through grain boundaries, where it reacts with the internal PbI_2 to form $MAPbI_3$ films. However, MAI tends to react preferentially with surface PbI_2, forming a perovskite layer that hinders further infiltration and prevents complete reaction with the underlying PbI_2. This incomplete conversion can result in high density of defects states within the perovskite films, degrading its overall quality and performance. In addition, the two-step fabrication process generally requires prolonged high-temperature annealing, which may cause the surface MAI to evaporate before fully penetrating the film [40, 41]. This further increases defect density and adversely affects perovskite crystallinity. According to previous reports on perovskite solar cells, Lewis base can promote perovskite crystallization during the two-step fabrication process, reduce defect concentrations, and improve photoelectric conversion efficiency [42].

As illustrated in Fig. 1(c), the addition of urea to the MAI solution facilitates the formation of an $MAI{\cdot}PbI_2{\cdot}O{=}C(NH_2)_2$ adduct, which moderates the reaction between MAI and PbI_2. This retardation allows deep MAI infiltration and complete reaction with internal PbI_2. Figures 1(d) and 1(e) show the scanning electron microscopy (SEM) images of the conventional and urea-optimized $MAPbI_3$ film surfaces (cross-sectional SEM images are provided in Fig. S2 in the ESM). The conventional $MAPbI_3$ films exhibit a smaller average grain size of 255 nm, whereas films treated with 1 mg/mL urea display larger and more uniformly distributed grains with tightly connected boundaries and an average grain size of 908 nm. Furthermore, energy-dispersive X-ray spectroscopy (EDS) elemental mapping supports the compositional uniformity of the films, as shown in Fig. S3 in the ESM. In addition, the atomic force microscopy (AFM) images and average grain size statistics for perovskite films with varying urea concentrations are provided in Fig. S4 in the ESM. Notably, excessive urea (e.g., 10 mg/mL) degrades the film morphology, likely due to its over-coordination with the PbI_2 precursor and the possible retention of insulating residues at grain boundaries. Typically, larger grain sizes correspond to fewer grain boundaries, which are known to be primary sites for shallow-level defects. Therefore, the addition of urea increases the grain size of the perovskite films, reduces grain boundaries, and effectively lowers defect density.

2.2 Optical properties of perovskite film

To investigate the mechanism by which urea regulates the crystallization process of $MAPbI_3$, we conducted Fourier-transform infrared (FTIR) spectroscopy and X-ray photoelectron spectroscopy (XPS) characterizations of perovskite films prepared via a two-step method at different reaction stages. The samples analyzed included the pure urea, PbI_2-MAI complex, urea-PbI_2-MAI complex, fully annealed $MAPbI_3$, and $MAPbI_3$ with urea additive. As shown in Fig. 2(a), the C=O stretching vibration peak of urea appears at 1675 cm^{-1}, and this characteristic peak is observed only in the $MAI{\cdot}PbI_2{\cdot}O{=}C(NH_2)_2$ complex. This result is consistent with the XRD spectra, which showed no shift in diffraction peaks upon the addition of urea. Moreover, as shown in Fig. 2(b), the C=O stretching vibration peak of the $MAI{\cdot}PbI_2{\cdot}O{=}C(NH_2)_2$ complex shifts from 1675 to 1666 cm^{-1}. According to the diatomic harmonic oscillator model [43], the vibrational frequency is proportional to the force constant. The observed red shift in the C=O stretching frequency indicates a decrease in the force constant. This can be attributed to the coordination between the Lewis base O^{2-} and the Lewis acid Pb^{2+}, which causes partial electron density transfer from C=O bond to the O–Pb interaction, thereby weakening the C=O bond strength. Consistently, the XPS analysis reveals a decrease in the binding energies of I 3d and Pb 4f in the urea-optimized film (Fig. S5 in the ESM), further supporting the coordination-mediated passivation of under-coordinated Pb^{2+} [44]. These results confirm that the urea enhances $MAPbI_3$ film quality through a synergistic

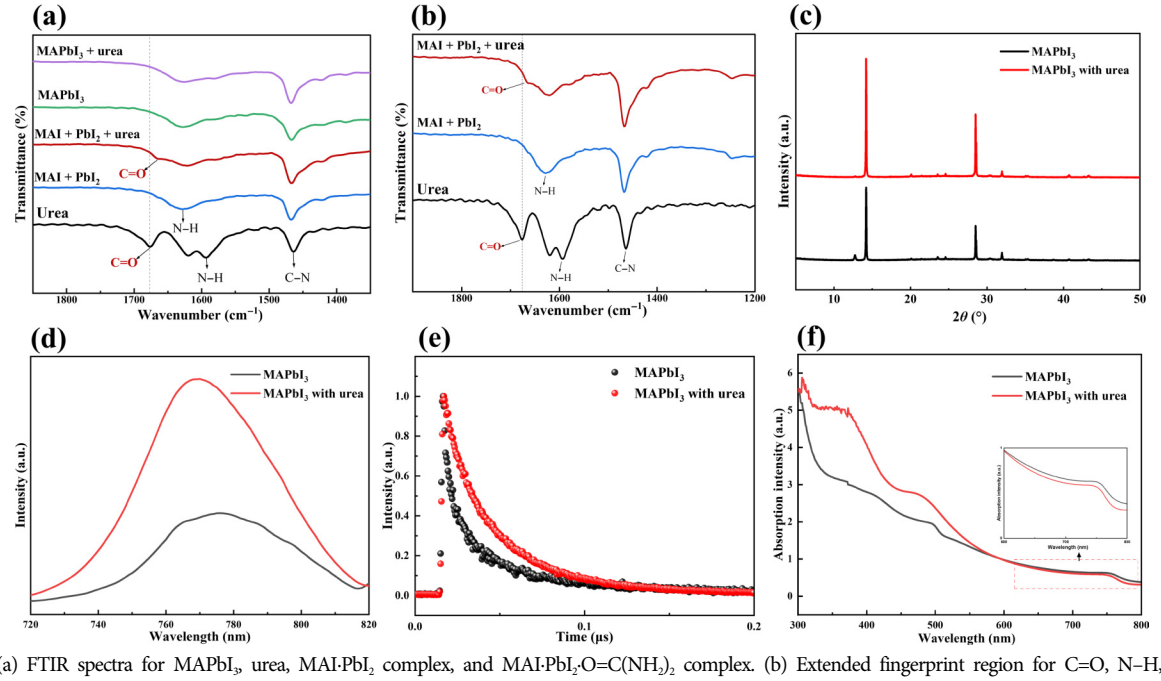

Figure 2 (a) FTIR spectra for $MAPbI_3$, urea, $MAI{\cdot}PbI_2$ complex, and $MAI{\cdot}PbI_2{\cdot}O{=}C(NH_2)_2$ complex. (b) Extended fingerprint region for C=O, N–H, and C–N vibrations. (c) XRD patterns of conventional and urea-optimized perovskite crystals. (d) Steady-state PL, (e) TRPL decay, and (f) absorption spectra of conventional and urea-optimized perovskite films. The urea concentration was 1 mg/mL in all urea-optimized $MAPbI_3$ film.

effect of grain growth, which reduces grain-boundary defects, and chemical passivation at the grain boundaries.

The structural and optical properties of conventional and urea-optimized $MAPbI_3$ perovskite films were characterized using X-ray diffraction (XRD), photoluminescence (PL), time-resolved photoluminescence (TRPL), and ultraviolet–visible (UV–vis) absorption spectroscopy. Figure 2(c) compares the XRD patterns of $MAPbI_3$ films prepared with and without urea additive. The diffraction peaks at 14.1°, 28.4°, 40.5°, and 43.1° correspond to the (110), (220), (224), and (314) crystal planes of the tetragonal perovskite structure, respectively [45, 46]. Notably, the urea-optimized $MAPbI_3$ films show significantly enhanced diffraction peaks in the (110) and (220) planes, indicating improved crystallinity of the perovskite crystals. In addition, no shift in the diffraction angles is observed, suggesting that the lattice structure remains unaltered upon urea incorporation. Figure 2(d) shows the PL spectra of the conventional and urea-optimized $MAPbI_3$ films. The figure shows that the PL spectrum of the urea-optimized $MAPbI_3$ film has a stronger peak intensity, indicating a reduction in defect density at the grain boundaries. These changes effectively suppress non-radiative recombination, thereby improving carrier transport and collection efficiency.

The TRPL spectroscopy was employed to study the carrier lifetime dynamic of the perovskite films, as shown in Fig. 2(e). The TRPL decays of both films were fitted using a biexponential model. The untreated film exhibits fast (τ_1) and slow (τ_2) decay components of 7.79 and 53.93 ns, respectively, with an average carrier lifetime of 23.94 ns. In contrast, the urea-optimized film shows prolonged lifetimes, with τ_1 = 25.78 ns, τ_2 = 68.5 ns, and an average lifetime of 37.30 ns. The extended carrier lifetime, particularly the notable increase in τ_1, indicates suppressed defect-assisted recombination, which can be attributed to the slowed crystallization process induced by urea addition, effectively reducing defect formation. Moreover, the urea-optimized $MAPbI_3$ film shows stronger light absorption compared to the conventional $MAPbI_3$ film (Fig. 2(f)). Considering that PbI_2 has a lower absorption in the visible light region compared to perovskite films [47], this result further confirms that the addition of urea promotes the complete reaction between PbI_2 and MAI during the two-step fabrication process and mitigates the absorption reduction caused by the accumulation of PbI_2 at the grain boundaries. Additionally, the increased grain size of the urea-optimized $MAPbI_3$ film may also contribute to the enhanced absorption intensity.

The space-charge-limited current (SCLC) is commonly used to study trap density in semiconductors, where a lower trap-filled-limit voltage (V_{TFL}) indicates a lower trap density [48]. Figure S6 in the ESM presents the SCLC measurements and calculated results for conventional and urea-treated $MAPbI_3$ films. The trap density of conventional film is 9.08×10^{15} cm^{-3}, which significantly decreases to 3.89×10^{15} cm^{-3} after urea optimization. The V_{TFL}-derived trap density results further confirm that the urea incorporation effectively reduces the defect density in $MAPbI_3$ films. The urea-optimized $MAPbI_3$ film shows improved charge separation, efficient photogenerated charge transport, and enhanced charge collection efficiency. These factors are crucial for achieving high-performance optoelectronic detection in photonic devices.

2.3 Photodetector properties

To further investigate the effect of urea on the optoelectronic conversion performance of $MAPbI_3$ films, we fabricated photodetector with device structure of Cu/C_{60}/bathocuproine (BCP)/$MAPbI_3$/poly(bis(4-phenyl) (2,4,6-trimethylphenyl)amine) (PTAA)/indium tin oxide (ITO), as shown in Fig. 3(a). The perovskite photodetectors were tested for their light response characteristics under zero bias using a 600 nm light source with a switching time of 2 s and an incident light intensity of 17.02 μW/cm^2. As shown in Fig. 3(b), compared to the conventional perovskite photodetector, the urea-optimized perovskite detector shows higher photocurrent and lower dark current, and the on/off ratio increased from 216 to 941, accompanied by a 30% improvement in sensitivity. The current density of the perovskite photodetectors as a function of incident light intensity (ranging from 0.26 to 17.02 μW/cm^2) is shown in Fig. 3(c). Both the conventional and urea-optimized perovskite photodetectors show good linear response characteristics, with the urea-optimized photodetectors showing higher current density under the same conditions.

For photodetectors, parameters such as responsivity, external quantum efficiency (EQE), and detectivity are critical for evaluating device performance. We systematically compared the responsivity, EQE, and detectivity of perovskite photodetectors under various incident light wavelengths at zero bias, as shown in Figs. 3(d)–3(f). The urea-optimized $MAPbI_3$ photodetectors exhibit excellent EQE across the visible light region, achieving a peak EQE of 82.89% at a wavelength of 500 nm. This is a significant improvement compared to the conventional $MAPbI_3$ photodetectors with a peak EQE of 59.26%. In addition, the urea-optimized photodetector shows significantly higher detectivity and responsivity over the entire wavelength range compared to the conventional device. Under 650 nm illumination with a light intensity of 17.02 μW/cm^2, the urea-optimized $MAPbI_3$ photodetectors achieve a responsivity of 0.45 A/W and a maximum detectivity of 2.5×10^{13} Jones. These performance improvements can be attributed to the effective passivation of defects in the $MAPbI_3$ films by urea, which substantially suppresses non-radiative carrier recombination and enhances charge collection efficiency.

2.4 Photon-counting detector performance

We constructed a pulsed light test system with calibrated light yield to evaluate the photon-counting performance of the conventional and urea-optimized $MAPbI_3$ photodetectors, as shown in Fig. 4(a). The system was driven by a pulse generator (Keysight 801150A), which triggered a light source to emit low-intensity pulsed 405 nm light. The light passed through an aperture and a set of neutral density filters with varying optical densities (OD) to achieve precise control over the output intensity. A diffusion plate was then employed to homogenize the beam, producing a uniform and adjustable light spot. The spot passed through a window with an optical output aperture of 2 mm × 2 mm, which defined the effective illumination area on photodetector and ensures consistent experimental conditions for all devices. The actual light output intensity was calibrated using a silicon photomultiplier (SiPM) based on the single-photon counting method (Fig. S7 in the ESM). All measurements were conducted in a light-tight enclosure, and the intrinsic noise of each detector was characterized separately as dark noise and incorporated into the photon-detection-resolution analysis. The primary uncertainties in the incident photon flux originated from the statistical fluctuation of the SiPM used for calibration and the tolerance in the OD values of the neutral density filters. To guarantee that each photodetector receives an identical photon flux under the same conditions, optical adhesive (Dow

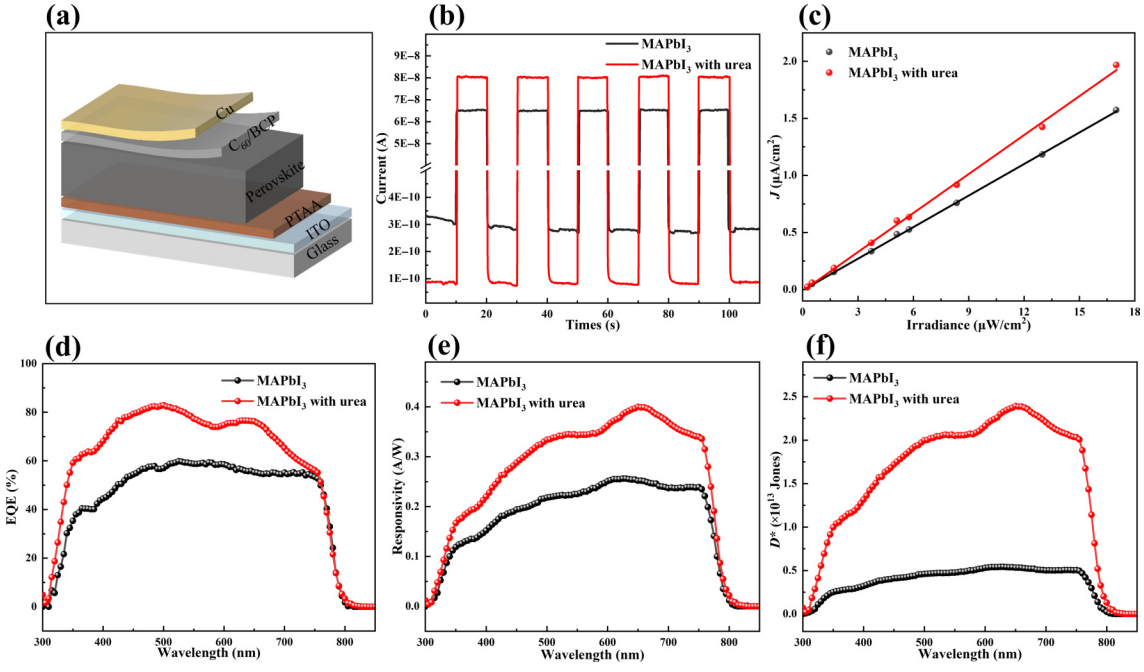

Figure 3 (a) Schematic diagram of the perovskite photodetector structure. (b) Time-dependent light response curves. (c) Current density at different light intensities. Curves showing (d) the variation of external quantum efficiency, (e) responsivity, and (f) detectivity of conventional and urea-optimized photodetector.

Corning) was used to couple the devices to the output window. The output signals from the photodetectors were amplified by a low-noise charge-sensitive amplifier (Kromek ev550) and acquired synchronously via a digital oscilloscope (Keysight DSOX6004A), with all instruments synchronized through LabVIEW-controlled pulse triggering and data acquisition. At a constant photon flux of 9.82×10^4 photon/mm^2 per light pulse, Fig. 4(b) presents the output signals from a charge-sensitive amplifier for silicon detector (biased at 100V) and self-powered perovskite photon-counting detector. Here, "self-powered" specifically means that the perovskite detector itself operates at zero external bias, while the subsequent readout electronics require an external power supply. Although the perovskite and silicon detectors (BPW34SR) differ in their physical mechanisms and operational modes, the perovskite detector exhibits a significantly larger pulse response amplitude under the described conditions, suggesting its superior charge collection efficiency for photon-counting applications. The histogram of the output signal responses for the perovskite photon-counting detector and silicon detector under varying incident light pulses is shown in Fig. 4(c). The perovskite detector shows higher peak channel number than silicon detector, which is consistent with the original waveform data. These results were highly reproducible across multiple devices, with relative standard deviations of the photocurrent and photon-counting response below 1% (Fig. S8 in the ESM). In addition, compared to the conventional perovskite detector, the urea-optimized perovskite photon-counting detector exhibits an increase in the number of peak channels and a reduction in noise, quantified by a decrease of 46% in the standard deviation (σ_{noise}) of the dark-noise histogram. This improvement in signal-to-noise characteristics shows a strong inverse correlation with the reduced trap density in the film (Figs. S9 and S10 in the ESM). It should be noted that the broader peak widths are primarily caused by the intrinsic noise of the detector with additional contributions from the fluctuation in photon generation by the light source.

As shown in Fig. 4(d), we further investigated the relationship between the detector response intensity and the number of incident photons under different conditions by plotting the peak channel number of the pulse statistical spectrum as a function of incident photon count. The results indicate that both silicon detector and self-powered perovskite photon-counting detector exhibit good linear response characteristics at low light intensities as the number of incident photons increases. Notably, the urea-optimized perovskite photon-counting detector demonstrates a response intensity that is 300% higher than that of the silicon detector. This improvement is attributed to the wide bandgap characteristics and excellent light absorption capabilities of the perovskite photon-counting detector, leading to more efficient optoelectronic conversion. To evaluate the performance of different detectors, we define a photon detection resolution (PDR) equation that quantifies the ability of a device to distinguish its pulse signal response from the dark noise signal under varying numbers of incident photons. A PDR value greater than 1 indicates that the pulse signal is fully distinguishable from the dark noise. The PDR is calculated as follows

$$\mathrm{PDR} = \frac{\mu_{\mathrm{PD}} - \mu_{\mathrm{noise}}}{2.354 \times (\sigma_{\mathrm{PD}} + \sigma_{\mathrm{noise}})} \quad (1)$$

where μ_{PD} denotes the mean of the impulse response signal histogram of the device at a given photon count, with σ_{PD} representing its standard deviation, and μ_{noise} refers to the mean of the histogram of the device's dark noise response in the absence of incident light, with σ_{noise} as its standard deviation.

Figure 4(e) illustrates the PDR as a function of incident photon number for silicon detector (under a bias of 100 V) and self-powered perovskite photon-counting detector. As the incident photon flux increases from 6.21×10^3 to 9.82×10^4 photons/mm^2, both devices exhibit a monotonic increase in PDR. Notably, the urea-optimized perovskite photon-counting detector achieves a significantly higher PDR across the entire range than the silicon photodetector. At an incident photon flux of 6.21 ×

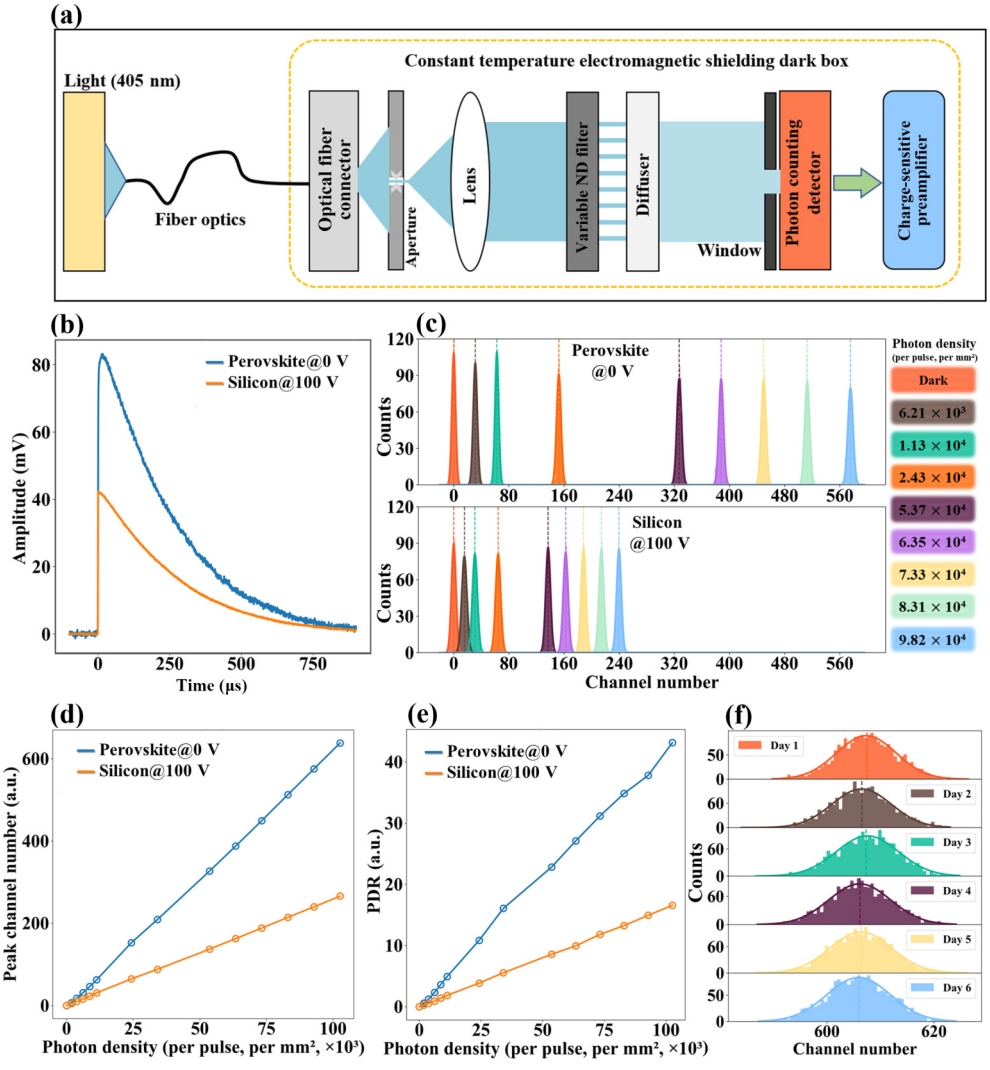

Figure 4 (a) Schematic of the photon counting system optical path. (b) Response pulse signals obtained from urea-optimized self-powered perovskite photon counting detector and silicon photodiodes at a bias of 100 V under the same incident photon flux. (c) Output signal histograms under incident light pulses with different photon numbers per pulse. (d) Photopeak channel number and (e) PDR for different numbers of incident photons per pulse. (f) Output signal histograms for the long-term response of the perovskite photon counting detector. The device was tested under constant photon flux in air (25 ± 2 °C; 30%RH ± 5%RH).

10^3 photons/mm^2, for instance, the PDR values are 0.92 for the silicon detector and 2.35 for the urea-optimized perovskite photon-counting detector. Theoretical calculations further determine the minimum detectable photon flux, defined as the flux required for a PDR of 1, where the optical response becomes fully distinguishable from the dark noise, to be 6.35 × 10^3 photons/mm^2 for the silicon photodetector and 2.01 × 10^3 photons/mm^2 for the perovskite detector. These results underscore the lower detection limit and superior sensitivity of the perovskite photon-counting detector. This enhanced performance is attributed to the excellent charge separation efficiency and outstanding optoelectronic conversion capability of the urea-optimized perovskite active layer. Moreover, the performance advantage of the perovskite detector becomes increasingly pronounced at higher incident light intensities.

Long-term operational stability is another critical metric for evaluating perovskite photon-counting detectors. The device, encapsulated with a glass coverslip using Norland Optical Adhesive 61 (UV-cured), was continuously tested under ambient laboratory conditions (25 ± 2 °C; 30%RH ± 5%RH) for seven days. We continuously monitored the detector response under a constant photon flux over seven days and recorded the corresponding output signal histograms (Fig. 4(f)). Owing to its effective self-powering operation, which significantly suppresses ion migration, the perovskite photon-counting detector exhibited negligible drift in the peak channel position and maintained a stable signal-to-noise ratio throughout the testing period. By eliminating the need for an external bias electric field, the self-powered perovskite detector avoids associated degradation mechanisms, thereby demonstrating good stability over the tested six-day period. This robust performance further confirms its strong potential for practical photon-counting applications, while further long-term and harsh-environment stability tests remain important for future deployment.

3 Conclusions

In this study, the defect density of $MAPbI_3$ films fabricated via a two-step method was significantly reduced by incorporating urea into the precursor solution. The trap density decreased from 9.08 × 10^{15} cm^{-3} in untreated films to 3.89 × 10^{15} cm^{-3} after urea optimization. Morphological, structural, and optoelectrical characterizations reveal that the urea-modified $MAPbI_3$ films exhibit larger grain

sizes, reduced grain boundary defects, and effective passivation of shallow-level defects. At zero bias under 600 nm illumination with an intensity of 17.02 μW/cm^2, the urea-optimized perovskite device achieved a responsivity of 0.45 A/W and a specific detectivity of 2.5 × 10^{13} Jones, significantly outperforming the conventional perovskite detector. In photon-counting tests, the urea-optimized perovskite photon-counting detector exhibited a pulse response amplitude three times greater than that of a silicon detector under identical conditions. Moreover, its minimum detectable photon flux was determined to be 2.01 × 10^3 photons/mm^2, substantially lower than the 6.35 × 10^3 photons/mm^2 of the silicon detector. The self-powered perovskite photon-counting detector also maintained stable response signals throughout the six-day testing period. This study demonstrates that the defect suppression in $MAPbI_3$ films via urea additive during two-step fabrication markedly enhances their optoelectronic performance, yielding a perovskite photodetector with superior photon-counting capability over silicon-based detectors. These findings offer new insights into defect roles in perovskite photon-counting devices and highlight molecular design for defect passivation as an effective optimization strategy. Future work may extend this approach to other perovskite compositions (e.g., FA/Cs-based and low-dimensional) and device architectures.

Electronic Supplementary Material: Supplementary material (detailed experimental procedures, material synthesis and device fabrication processes, additional structural and morphological characterizations, surface chemical analysis, optical properties, electrical measurements, and extended photon-counting performance data and analysis) is available in the online version of this article at https://doi.org/10.26599/NR.2026.94908490.

Data availability

All data needed to support the conclusions in the paper are presented in the manuscript and the Electronic Supplementary Material. Additional data related to this paper may be requested from the corresponding author upon request.

Acknowledgements

This work was financially supported by the National Key Research and Development Program of China (No. 2022YFE0118400), the Shenzhen Medical Research Fund (No. D250402005), the National Natural Science Foundation of China (Nos. 62474187, 12235006, 62174078, 62404237, and 12375358), the Shenzhen Basic Research Program (Nos. JCYJ20220818101612027 and JCYJ20241202124959 61), the Natural Science Foundation of Hunan Province (No. 2022RC1076), and Guangdong Basic and Applied Basic Research Foundation (Nos. 2022B1515020029 and 2024A1515012494).

Declaration of competing interest

All the contributing authors report no conflict of interests in this work.

Author contribution statement

W. J. L. and P. S. G.: Conceptualization, methodology, investigation, data curation, formal analysis, writing – review & editing. B. Y. H., K. X. H., X. Z. S., and W. X. Y.: Investigation, data curation, validation. Q. Z., H. H., Y. Z., X.-F. Y., and Y. F. Y.: Project administration, funding acquisition. C. L., Z. L., W. H. Z., and Y. L. L.: Project administration, funding acquisition, writing – review & editing. All the authors have approved the final manuscript.

Use of AI statement

None.

References

[1] Hadfield, R. H. Single-photon detectors for optical quantum information applications. *Nat. Photon.* **2009**, *3*, 696–705.
[2] Gundacker, S.; Heering, A. The silicon photomultiplier: Fundamentals and applications of a modern solid-state photon detector. *Phys. Med. Biol.* **2020**, *65*, 17TR01.
[3] Koppens, F. H. L.; Mueller, T.; Avouris, P.; Ferrari, A. C.; Vitiello, M. S.; Polini, M. Photodetectors based on graphene, other two-dimensional materials and hybrid systems. *Nat. Nanotechnol.* **2014**, *9*, 780–793.
[4] Li, J. H.; Niu, L. Y.; Zheng, Z. J.; Yan, F. Photosensitive graphene transistors. *Adv. Mater.* **2014**, *26*, 5239–5273.
[5] Liu, Y. J.; Ji, Z. Single-pixel color imaging based on a high-performance $MAPbI_3$ perovskite photodetector. *Appl. Phys. Lett.* **2023**, *122*, 021103.
[6] Wang, F.; Zou, X. M.; Xu, M. J.; Wang, H.; Wang, H. L.; Guo, H. J.; Guo, J. X.; Wang, P.; Peng, M.; Wang, Z. et al. Recent progress on electrical and optical manipulations of perovskite photodetectors. *Adv. Sci.* **2021**, *8*, 2100569.
[7] Kim, W.; Kim, H.; Yoo, T. J.; Lee, J. Y.; Jo, J. Y.; Lee, B. H.; Sasikala, A. A.; Jung, G. Y.; Pak, Y. Perovskite multifunctional logic gates via bipolar photoresponse of single photodetector. *Nat. Commun.* **2022**, *13*, 720.
[8] Feng, X. P.; He, Y. H.; Qu, W.; Song, J. M.; Pan, W. T.; Tan, M. R.; Yang, B.; Wei, H. T. Spray-coated perovskite hemispherical photodetector featuring narrow-band and wide-angle imaging. *Nat. Commun.* **2022**, *13*, 6106.
[9] Im, J. H.; Jang, I. H.; Pellet, N.; Grätzel, M.; Park, N. G. Growth of $CH_3NH_3PbI_3$ cuboids with controlled size for high-efficiency perovskite solar cells. *Nat. Nanotechnol.* **2014**, *9*, 927–932.
[10] Jeon, N. J.; Noh, J. H.; Kim, Y. C.; Yang, W. S.; Ryu, S.; Seok, S. I. Solvent engineering for high-performance inorganic–organic hybrid perovskite solar cells. *Nat. Mater.* **2014**, *13*, 897–903.
[11] Bi, D. Q.; Tress, W.; Dar, M. I.; Gao, P.; Luo, J. S.; Renevier, C.; Schenk, K.; Abate, A.; Giordano, F.; Baena, J. P. C. et al. Efficient luminescent solar cells based on tailored mixed-cation perovskites. *Sci. Adv.* **2016**, *2*, e1501170.
[12] Lee, M. M.; Teuscher, J.; Miyasaka, T.; Murakami, T. N.; Snaith, H. J. Efficient hybrid solar cells based on meso-superstructured organometal halide perovskites. *Science* **2012**, *338*, 643–647.
[13] Bi, D. Q.; Yi, C. Y.; Luo, J. S.; Décoppet, J. D.; Zhang, F.; Zakeeruddin, S. M.; Li, X.; Hagfeldt, A.; Grätzel, M. Polymer-templated nucleation and crystal growth of perovskite films for solar cells with efficiency greater than 21%. *Nat. Energy* **2016**, *1*, 16142.
[14] Sun, S. Y.; Salim, T.; Mathews, N.; Duchamp, M.; Boothroyd, C.; Xing, G. C.; Sum, T. C.; Lam, Y. M. The origin of high efficiency in low-temperature solution-processable bilayer organometal halide hybrid solar cells. *Energy Environ. Sci.* **2014**, *7*, 399–407.
[15] Ponseca, C. S. Jr.; Savenije, T. J.; Abdellah, M.; Zheng, K. B.; Yartsev, A.; Pascher, T.; Harlang, T.; Chabera, P.; Pullerits, T.; Stepanov, A. et al. Organometal halide perovskite solar cell materials rationalized: Ultrafast charge generation, high and microsecond-long balanced mobilities, and slow recombination. *J. Am. Chem. Soc* **2014**, *136*, 5189–5192.
[16] Dong, Q. F.; Fang, Y. J.; Shao, Y. C.; Mulligan, P.; Qiu, J.; Cao, L.; Huang, J. S. Solar cells. Electron–hole diffusion lengths > 175 μm in solution-grown $CH_3NH_3PbI_3$ single crystals. *Science* **2015**, *347*, 967–970.

[17] Shi, D.; Adinolfi, V.; Comin, R.; Yuan, M. J.; Alarousu, E.; Buin, A.; Chen, Y.; Hoogland, S.; Rothenberger, A.; Katsiev, K. et al. Solar cells. Low trap-state density and long carrier diffusion in organolead trihalide perovskite single crystals. *Science* **2015**, *347*, 519–522.

[18] Lim, K. G.; Ahn, S.; Kim, Y. H.; Qi, Y. B.; Lee, T. W. Universal energy level tailoring of self-organized hole extraction layers in organic solar cells and organic-inorganic hybrid perovskite solar cells. *Energy Environ. Sci.* **2016**, *9*, 932–939.

[19] Stranks, S. D.; Eperon, G. E.; Grancini, G.; Menelaou, C.; Alcocer, M. J. P.; Leijtens, T.; Herz, L. M.; Petrozza, A.; Snaith, H. J. Electron–hole diffusion lengths exceeding 1 micrometer in an organometal trihalide perovskite absorber. *Science* **2013**, *342*, 341–344.

[20] Xing, G. C.; Mathews, N.; Sun, S. Y.; Lim, S. S.; Lam, Y. M.; Grätzel, M.; Mhaisalkar, S.; Sum, T. C. Long-range balanced electron- and hole-transport lengths in organic-inorganic $CH_3NH_3PbI_3$. *Science* **2013**, *342*, 344–347.

[21] Qin, L. N.; Zhu, M. F.; Xia, Y. R.; Ma, X. K.; Hong, D. C.; Tian, Y. X.; Tie, Z. X.; Jin, Z. Multifunctional dual-anion compensation of amphoteric glycine hydrochloride enabled highly stable perovskite solar cells with prolonged carrier lifetime. *Nano Res.* **2024**, *17*, 5131–5137.

[22] D'Innocenzo, V.; Grancini, G.; Alcocer, M. J. P.; Kandada, A. R. S.; Stranks, S. D.; Lee, M. M.; Lanzani, G.; Snaith, H. J.; Petrozza, A. Excitons versus free charges in organo-lead tri-halide perovskites. *Nat. Commun.* **2014**, *5*, 3586.

[23] Ran, C. X.; Xu, J. T.; Gao, W. Y.; Huang, C. M.; Dou, S. X. Defects in metal triiodide perovskite materials towards high-performance solar cells: Origin, impact, characterization, and engineering. *Chem. Soc. Rev.* **2018**, *47*, 4581–4610.

[24] Green, M. A.; Ho-Baillie, A.; Snaith, H. J. The emergence of perovskite solar cells. *Nat. Photon.* **2014**, *8*, 506–514.

[25] Park, N. G. Perovskite solar cells: An emerging photovoltaic technology. *Mater. Today* **2015**, *18*, 65–72.

[26] Zhao, Y. X.; Zhu, K. Organic-inorganic hybrid lead halide perovskites for optoelectronic and electronic applications. *Chem. Soc. Rev.* **2016**, *45*, 655–689.

[27] Zhou, Y.; Fei, C. B.; Uddin, M. A.; Zhao, L.; Ni, Z. Y.; Huang, J. S. Self-powered perovskite photon-counting detectors. *Nature* **2023**, *616*, 712–718.

[28] Cao, H. Y.; Cheng, W. Y.; Wang, C.; Li, L. T.; Wang, R. N.; Sun, X. L.; Lai, H. H.; Feng, X. K.; Zhang, F. C.; Zou, G. F. Metal halide perovskite single-crystal thin films: From films growth to light-emitting application. *Small Methods* **2025**, *9*, 2401861 .

[29] Du, X. R.; Li, Y.; Yu, Z. K.; Oh, C. M.; Zhang, Y. Y.; Liu, F. W.; Yang, E.; Ahn, Y.; Chen, Y. Z. et al. Multi-functional ion-pairing additive for efficient quasi-2D perovskite light-emitting diodes and solar cells. *Chem. Eng. J.* **2024**, *487*, 150596.

[30] Liu, J.; Cai, W. X.; Shang, W. Z.; Li, W. R.; Wang, S. H.; Cai, W. Q.; Shi, Y. T.; Wang, Y. D. Polymer-assisted crystal growth regulation and defect passivation for efficient perovskite solar cells. *Appl. Phys. Lett.* **2024**, *125*, 113506.

[31] Sun, J. Y.; Liu, N.; Zhang, L.; Zhang, C.; Liu, K.; Sun, Q. Z.; Gao, K. W.; Shao, Y.; Chen, X. Y.; Qiu, F. Z. Multi-functional interface repair strategy for high performance $FAPbI_3$ photodetectors. *J. Alloys Compd.* **2025**, *1015*, 178894.

[32] Sun, D. Y.; Peng, M.; Wang, T. J.; Yi, L. J.; Zhang, S. Z.; Liu, F.; Cheng, G. J. Leflunomide: A versatile additive for defect reduction, enhanced optoelectronic properties and environmental stability of perovskite films. *Nano Res.* **2024**, *17*, 2628–2637.

[33] Wetzelaer, G. J. A. H.; Scheepers, M.; Sempere, A. M.; Momblona, C.; Ávila, J.; Bolink, H. J. Trap-assisted non-radiative recombination in organic–inorganic perovskite solar cells. *Adv. Mater.* **2015**, *27*, 1837–1841.

[34] Leijtens, T.; Eperon, G. E.; Barker, A. J.; Grancini, G.; Zhang, W.; Ball, J. M.; Kandada, A. R. S.; Snaith, H. J.; Petrozza, A. Carrier trapping and recombination: The role of defect physics in enhancing the open circuit voltage of metal halide perovskite solar cells. *Energy Environ. Sci.* **2016**, *9*, 3472–3481.

[35] Conwell, E.; Weisskopf, V. F. Theory of impurity scattering in semiconductors. *Phys. Rev.* **1950**, *77*, 388–390.

[36] Yuan, Y. B.; Huang, J. S. Ion migration in organometal trihalide perovskite and its impact on photovoltaic efficiency and stability. *Acc. Chem. Res.* **2016**, *49*, 286–293.

[37] Queisser, H. J.; Haller, E. E. Defects in semiconductors: Some fatal, some vital. *Science* **1998**, *281*, 945–950.

[38] Zhao, J. H.; Wang, A. H.; Green, M. A.; Ferrazza, F. 19.8% efficient "honeycomb" textured multicrystalline and 24.4% monocrystalline silicon solar cells. *Appl. Phys. Lett.* **1998**, *73*, 1991–1993.

[39] Geisz, J. F.; Kurtz, S.; Wanlass, M. W.; Ward, J. S.; Duda, A.; Friedman, D. J.; Olson, J. M.; McMahon, W. E.; Moriarty, T. E.; Kiehl, J. T. High-efficiency GaInP/GaAs/InGaAs triple-junction solar cells grown inverted with a metamorphic bottom junction. *Appl. Phys. Lett.* **2007**, *91*, 023502.

[40] Turren-Cruz, S. H.; Hagfeldt, A.; Saliba, M. Methylammonium-free, high-performance, and stable perovskite solar cells on a planar architecture. *Science* **2018**, *362*, 449–453.

[41] Zheng, X. P.; Chen, B.; Dai, J.; Fang, Y. J.; Bai, Y.; Lin, Y. Z.; Wei, H. T.; Zeng, X. C.; Huang, J. S. Defect passivation in hybrid perovskite solar cells using quaternary ammonium halide anions and cations. *Nat. Energy* **2017**, *2*, 17102.

[42] Tian, C. B.; Zhang, S. J.; Mei, A. Y.; Rong, Y. G.; Hu, Y.; Du, K.; Duan, M.; Sheng, Y. S.; Jiang, P.; Xu, G. Z. et al. A multifunctional bis-adduct fullerene for efficient printable mesoscopic perovskite solar cells. *ACS Appl. Mater. Interfaces* **2018**, *10*, 10835–10841.

[43] Ahn, N.; Son, D. Y.; Jang, I. H.; Kang, S. M.; Choi, M.; Park, N. G. Highly reproducible perovskite solar cells with average efficiency of 18.3% and best efficiency of 19.7% fabricated via lewis base adduct of lead(II) iodide. *J. Am. Chem. Soc.* **2015**, *137*, 8696–8699.

[44] Huang, Z. Q.; Hu, X. T.; Liu, C.; Tan, L. C.; Chen, Y. W. Nucleation and crystallization control via polyurethane to enhance the bendability of perovskite solar cells with excellent device performance. *Adv. Funct. Mater.* **2017**, *27*, 1703061.

[45] Hsu, H. L.; Hsiao, H. T.; Juang, T. Y.; Jiang, B. H.; Chen, S. C.; Jeng, R. J.; Chen, C. P. Carbon nanodot additives realize high-performance air-stable p–i–n perovskite solar cells providing efficiencies of up to 20.2%. *Adv. Energy Mater.* **2018**, *8*, 1802323.

[46] Wang, R.; Xue, J. J.; Meng, L.; Lee, J. W.; Zhao, Z. P.; Sun, P. Y.; Cai, L.; Huang, T. Y.; Wang, Z. X.; Wang, Z. K. et al. Caffeine improves the performance and thermal stability of perovskite solar cells. *Joule* **2019**, *3*, 1464–1477.

[47] Wang, S.; Ma, Z. R.; Liu, B. B.; Wu, W. C.; Zhu, Y.; Ma, R. X.; Wang, C. Y. High-performance perovskite solar cells with large grain-size obtained by using the lewis acid-base adduct of thiourea. *Solar RRL* **2018**, *2*, 1800034.

[48] Le Corre, V. M.; Duijnstee, E. A.; El Tambouli, O.; Ball, J. M.; Snaith, H. J.; Lim, J.; Koster, L. J. A. Revealing charge carrier mobility and defect densities in metal halide perovskites via space-charge-limited current measurements. *ACS Energy Lett.* **2021**, *6*, 1087–1094.